ADVANCED FUNCTIONAL MATERIALS

DOI: 10.1002/adfm.200700314

Excitonic and Vibrational Properties of Single-Walled Semiconducting Carbon Nanotubes**

By *Svetlana Kilina* and *Sergei Tretiak**

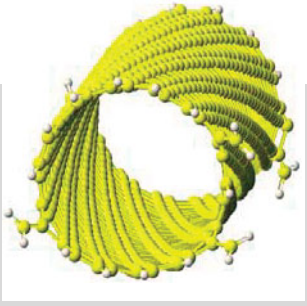

We review quantum-chemical studies of the excited-state electronic structure of finite-size semiconducting single-walled carbon nanotubes (SWCNTs) using methodologies previously successfully applied to describe conjugated polymers and other organic molecular materials. The results of our simulations are in quantitative agreement with available spectroscopic data and show intricate details of excited-state properties and photoinduced vibrational dynamics in carbon nanotubes. We analyze in detail the nature of strongly bound first and second excitons in SWCNTs for a number of different tubes, emphasizing emerging size-scaling laws. Characteristic delocalization properties of excited states are identified by the underlying photoinduced changes in charge densities and bond orders. Due to the rigid structure, exciton–phonon coupling is much weaker in SWCNTs compared to typical molecular materials. Yet we find that, in the ground state, a SWCNT's surface experiences the corrugation associated with electron–phonon interactions. Vibrational relaxation following photoexcitation reduces this corrugation, leading to a local distortion of the tube surface, which is similar to the formation of self-trapped excitons in conjugated polymers. The calculated associated Stokes shift increases with enlargement of the tube diameters. Such exciton vibrational phenomena are possible to detect experimentally, allowing for better understanding of photoinduced electronic dynamics in nanotube materials.

1. Introduction

Rapid advances in chemical synthesis and fabrication techniques generate novel types of nanometer-sized materials that exhibit original and often unforeseen properties, which can be controlled not only by the type of material but also by sample size, shape, and topology. Carbon nanotubes are one of the brightest examples of such materials. Single-walled carbon nanotubes (SWCNTs) can be considered as quasi-one-dimensional derivatives of bulk graphite; whereby one-atom-thick layers are rolled into long rigid cylinders a few nanometers in diameter.[1–3] The diameter and direction of the tube's rolling (a chiral vector (n,m)) define the main features of SWCNTs, such as a semiconductor or metal-like electronic structure. SWCNTs are in neither the bulk semiconductor nor molecular regime, and exhibit an entirely new range of properties, placing them in between the two traditional types of materials. Their extraordinary mechanical, electronic, and optical properties, as well as an ability to tune these properties by a tube's geometry, make SWCNTs very promising materials for a number of tech-

[*] S. Kilina, Dr. S. Tretiak
Theoretical Division and Center for Nonlinear Studies (CNLS), and Center for Integrated Nanotechnologies (CINT)
Los Alamos National Laboratory
Los Alamos, NM 87545 (USA)
E-mail: serg@lanl.gov
S. Kilina
Department of Chemistry, University of Washington
Seattle, WA 98195-1700 (USA)

[**] The authors thank A. P. Shreve, S. K. Doorn, V. Klimov, G. Lanzani, A. Jorio, A. Piryatinski, A. Saxena, R. L. Martin, and A. R. Bishop for valuable discussion. S.K. thanks Oleg Prezhdo for fruitful discussions and the University of Washington Department of Chemistry for computer resources. The research at LANL is supported by the Center for Integrated Nanotechnology (CINT) and Center for Nonlinear Studies (CNLS). Los Alamos National Laboratory is operated by Los Alamos National Security, LLC, for the National Nuclear Security Administration of the U.S. Department of Energy under contract DE-AC52-06NA25396. This support is gratefully acknowledged.

nological applications. The potential applications include but are not limited to chemical sensors[4,5] and mass conveyers,[6] nanoscale logic gates[7,8] and antennas,[9] conductor switches,[10,11] lasers,[12,13] field-effect transistors,[14,15] and logic circuits.[16]

Many of the above applications and fundamental studies require manipulation of one particular type of a tube with a well-determined diameter and chiral vector. For instance, the bandgap of a semiconducting tube, a critical parameter that needs to be controlled for nanoelectronic applications, is strongly dependent on tube geometry. From the experimental standpoint, however, the specification of individual SWCNTs is difficult because the tubes of different species, orientations, and lengths are mixed together in one sample. Tube polydispersion (bundling), poor solubility, and defects complicate the problem even further. Modern catalysts and growth processes allow control of the diameter of synthesized nanotubes to some degree. Samples have been enriched[17] or separated into pure metallic and semiconductor fractions using dielectrophoresis[18,19] or through selective reaction chemistry.[18] Separations of individual semiconductor chiralities have been relatively successful using DNA-wrapping chemistry or reversible chirality-selective CNT redox chemistry[20] that yields enriched samples of only a single large bandgap chirality.[21] In spite of these advances, obtaining specific defect-free chiral SWCNT species remains a huge challenge for synthesis and technology.

Spectroscopic techniques are currently the mainstream approach to provide precise characterization of SWCNT samples. Sophisticated combinations of absorption, fluorescence, and Raman spectroscopies[22–25] make the assignment of a type of tube routine. The main component of these techniques is spectroscopic identification of the tube diameter and the optical transition energies E_{ii} that specify individual (n,m) nanotubes. Resonant Raman spectroscopy[26–28] delivers an accurate identification of tube diameters and transition energies in a homogeneous sample by measuring the radial breathing mode (RBM) frequency. Complementary photoluminescence (PL) experiments provide $(n-m)$, $(2n+m)$, and $(2m+n)$ family behavior of E_{22} absorption peaks and E_{11} emission peaks, which identify well an individual (n,m) tube in a suspension. Yet, the spectroscopic tube identification is still a challenge because of inhomogeneous broadening, spectral overlap, and relatively low efficiency of PL spectra, which cause complications in (n,m) assignment.

New synthetic advances and applications of sophisticated experimental approaches resulted in revolutionary re-evaluation of the basic photophysics of SWCNTs over the past five years. Early optical spectra in SWCNTs had been interpreted in terms of free electron–hole carriers. Indeed, the electronic structure of SWCNTs, predicted by tight-binding Hamiltonian models, provides equally spaced sub-bands of valence and conduction bands with diverging density of states at the edges, known as van Hove singularities, which result from one-dimensional (1D) confinement conditions.[1] Recent transient spectroscopy and nonlinear absorption data[29–31] have unambiguously revealed that the photophysics of SWCNTs is dominated by strongly bound excitons (interacting electron–hole pairs) rather than free particles. Measurement of the excitonic bind-

Svetlana Kilina received her B.Sc. and M.Sc. in Physics from Belarus State University (1996). She taught physics in Belarus, including preparing children to compete in the National Physics Olympics. She spent three years at Chemnitz University of Technology, Germany, as a research assistant studying the transportation properties of disordered interacting electrons. She began her Ph.D. in Physical Chemistry at the University of Washington in 2003, during which she has been working as a research assistant at Los Alamos National Laboratory. Her research focuses on photoinduced electron–phonon dynamics in nanoscale systems, such as quantum dots, carbon nanotubes, conjugated polymers, and DNA materials.

Sergei Tretiak received his M.Sc. (1994) from Moscow Institute of Physics and Technology, and his Ph.D. (1998) from the University of Rochester, where he worked with Prof. S. Mukamel. He subsequently became a Technical Staff Member (2001–present) at Los Alamos National Laboratory. Since 2006, he is a member of the DOE-funded Center for Integrated Nanotechnologies (CINT). His research interests include development of modern computational methods for molecular optical properties; time-dependent density functional theory and semiempirical methods; nonlinear optical response of organic chromophores; adiabatic and nonadiabatic molecular dynamics of the excited states; collective electronic excitations and optical response of confined excitons in various materials; charge and energy transfer in biological and artificial antenna complexes; ultrafast nonlinear spectroscopy.

ing energy was done using two-photon excitation spectroscopy[32,33] and pump-probe spectroscopy.[34] Taking advantage of allowed and well-defined transitions to both the bound exciton state and to the near-continuum unbound states, the binding energy of approximately 0.4 eV for the first excitonic band (E_{11}) in semiconducting SWCNTs with 0.8 nm diameters was determined. This is about one hundred times larger than that for bulk semiconductors, but comparable to other 1D materials, such as conjugated polymers.[35] Measurement of the binding energy of the second excitonic band E_{22} by resonant Raman scattering provides even higher values of about 0.5 eV and 0.6 eV for (10,3) and (7,5) tubes, respectively.[36] Starting from the pioneering study by Ando,[37] a large amount of theoretical work has confirmed strong excitonic effects in SWCNTs.[38–42] These results demonstrate that, unlike in bulk systems, the excited-state properties of nanotubes are dominated by many-body interactions, which is a typical scenario for many nanoscale materials.[35] Thus, excitonic effects can not be largely neglected or treated as a small perturbation to the bandgap of SWCNTs as it was assumed in earlier studies.

In addition to the excitonic features, vibronic resonances in the photoluminescence excitation spectra,[43,44] vibrational progression in absorption/fluorescence lineshapes,[45,46] Raman spectroscopy,[28,47,48] coherent phonon excitation experiments,[49,50] transport measurements,[51] as well as theoretical studies[52–57] have brought evidence of significant carrier–phonon interaction in SWCNTs. It is important to note that both electron–electron and electron–phonon interactions are typical features of low-dimensional systems,[35] such as conjugated organic[58–60] and organometallic[61] polymers, mixed-valence chains,[62] and, in general, organic molecular materials.[63–65] However, nanotubes have a rigid structure and cannot be regarded as pure 1D systems because of their circumferential dimension. Subsequently, excitonic and vibrational effects in SWCNTs are expected to differ from that in the above systems and to be very sensitive to tube size and geometry. Quantitative measurements of electron–phonon coupling constants and Huang–Rhys factors from the analysis of experimental Raman profiles[66,67] and calculations[67,68] place SWCNTs in a regime of weak coupling strength, compared to typical molecular systems, but far exceeding electron–phonon coupling constants observed in semiconductor materials.

Thus, both excitonic and vibronic effects are equally important for a correct description of photoinduced dynamics in nanotubes. These phenomena need to be clearly understood to achieve proper functionalities of future nanotube-based electronic devices. Clearly, an accurate description of these features depends on a proper incorporation of both strong Coulomb and exciton–phonon couplings. Computational studies utilizing accurate quantum-chemical methods are complicated and usually involve significant numerical effort. Consequently, existing theoretical investigations based on rigorous first-principle methodologies focus on only one class of phenomena: either excitonic or vibrational. On the other hand, computations utilizing model Hamiltonian approaches have limited accuracy and do not include, for example, curvature-induced σ- and π-bond mixing and possible deviations from the sp^2 hybridization, which are important effects in the case of SWCNTs.[54,69–71]

One of the most accurate theoretical descriptions of excitonic effects in SWCNTs has been provided by a Green's functions approach via the solution of the Bethe–Salpeter equation (BSE) by adding self-energy corrections (*GW*) to the local-density approximation (LDA).[72] This method has demonstrated significant electron–electron interactions and has proved the dominating role of excitons in the optical spectra of SWCNTs.[39,42] The same BSE approach, but coupled to a much simpler empirical tight-binding Su–Schrieffer–Heeger (SSH) model, was fruitfully used to evaluate various excitonic properties,[73] size-scaling laws,[41] carrier transport,[74,75] and electron–phonon coupling effects[53] in a broad range of nanotube species. Density-functional theory (DFT) has also been widely used to calculate curvature and electron–phonon effects,[57,68] uncorrelated gaps,[76,77] and non-adiabatic electron–phonon dynamics.[52] Fewer applications of time-dependent DFT (TD-DFT) to SWCNT systems have been reported. The latter technique allows for adequate treatment of excitonic effects with accuracy comparable to BSE-based methods[72,78] and has currently become a mainstream approach for calculating electronic excitations in molecular materials. For example, the application of TD-DFT to narrow tubes[79] demonstrates surprisingly good agreement with experimental results and reveals the importance of depolarization effects.

The above-described theoretical approaches assume periodic boundary conditions to address long SWCNT lengths. Recently, a number of simulations using finite tube lengths has been reported.[34,40,49,55,80] These techniques use methodologies previously developed for molecular materials. Finite-size calculations are able to address all excitonic phenomena as once the molecular size becomes larger than the characteristic exciton size, all physical properties become additive. This means, for instance, a saturation to a constant of excitation energies. Consequently, a large enough molecule represents the infinite system limit well. Such techniques are routinely applied to many other 1D systems such as conjugated polymers or mixed-valence chains.[58,59,62,81–83] This brings broad experience and accurate theoretical methodologies, well-developed for the characterization of molecular systems, to SWCNTs. For example, calculations based on an empirical Pariser–Par–Pople (PPP) π-electron Hamiltonian approach[40] explain the low PL efficiency of SWCNTs because of intrinsic low-lying 'dark' excitonic states. The same approach indicated many common features in the electronic spectra of SWCNTs and conjugated polymers; a fact that was confirmed by transient absorption spectroscopic measurements.[34] We further note that group-theoretical analysis of optical selection rules based on the periodic boundary conditions in SWCNTs fails to predict their strong nonlinear absorption, which should be completely forbidden in theory but clearly shows up in two-photon PL[32,33] and transient absorption spectra.[34] In contrast, finite-tube calculations are able to explain the basic photophysics underlying these spectra well and to characterize the properties of the excited states involved.[34,84] Consequently, solid-state-like (periodic boundary conditions) and molecular-like (finite-size)

theoretical approaches are complementary in discovering the rich photophysics of SWCNT materials.

This Feature Article overviews an extensive study of both excitonic and vibrational effects in SWCNTs using finite-size molecular-type approaches. We use our excited-state molecular dynamics (ESMD) technique,[59,85] recently developed and successfully applied to many conjugated molecular materials.[60,86–89] This method makes simulations of exciton–vibrational dynamics in very large systems up to one thousand atoms in size possible, while retaining the necessary quantitative accuracy. This is achieved by combining three techniques: i) Reliable semiempirical all-valence approaches, such as Austin Model 1 (AM1)[90] or the intermediate neglect of differential overlap (INDO) model,[91] to treat natural curvature and vibrational effects at a significantly reduced computational complexity level compared to ab initio approaches; ii) A time-dependent Hartree–Fock (TDHF) approximation to address essential electronic correlations and excitonic effects. The TDHF, combined with Krylov subspace algorithms[92] in the collective electronic oscillator (CEO) code,[86] makes it possible to calculate hundreds of molecular excited states with only moderate numerical expense; iii) Finally, analytic gradients of the excited-state potential energy surfaces[93] in the ESMD package allow investigation of vibrational phenomena, excited-state optimizations, and dynamics.[85,89] We recently have used this technique to address several excited-state phenomena in SWCNTs, which have also been studied experimentally. This includes anharmonic coherent phonon dynamics,[49] quantification of exciton–phonon coupling and Huang–Rhys factors,[67] characterization of delocalized non-excitonic transitions (E_{33} and E_{44}),[94] and effects of Peierls distortion and exciton self-trapping.[55] Compared to selected SWCNT species used in the previous work, here we model in detail excited-state phenomena in ten chiral and five zigzag carbon nanotubes, focusing on the dependence of exciton–vibrational phenomena on tube chiralities and diameters ranging between 4 and 13 Å. Compared to model calculations, we expect to understand the interplay of π- and σ-bonding using our technique, as well as curvature and chirality effects in the excited states of SWCNTs.

This article is organized as follows. Details of our computational approach are presented in Section 2. In Section 3, we analyze the calculated excitonic structure and exciton–vibrational phenomena of SWCNTs. Finally, we discuss the trends that emerge and summarize our findings in Section 4.

2. Computational Methodology

2.1. Hamiltonian Model and Electronic Correlations

To study the exciton–vibrational phenomena in SWCNTs, we employed the following computational strategy. Ground-state optimal geometries were obtained using the Austin Model 1 (AM1) semiempirical Hamiltonian[90] at the Hartree–Fock (HF) level. The AM1 approach was specifically designed for this purpose and was widely applied to calculate ground-[95] and excited-state[88,96] properties of many molecular systems. This includes chemical energies, geometries, dipoles, excitation energies, and polarizabilities. The semiempirical approximation restricts the basis set to valence orbitals of Slater-type. This limits the number of computed Hamiltonian matrix elements and allows storage of all of them in memory, instead of recalculating them when needed, as is commonly done in ab initio computations.[97] This methodology makes semiempirical techniques significantly easier and faster yet allows for an accurate description of a broad range of electronic phenomena. For example, no assumptions to the vibrational properties and curvature-mediated σ- and π-interactions are necessary as the AM1 Hamiltonian has these effects built into the dependence of its matrix elements on the nuclei positions. This constitutes an important advantage over the simpler tight-binding π-electron empirical approximations such as PPP[34,40] or SSH[41,53,73] models.

Optimized ground-state geometries provide input structures for excited-state calculations performed using the CEO code combined with the AM1 Hamiltonian. The CEO approach, described in detail elsewhere,[59,86] solves the equation of motion for the single-electron density matrix[98] $\rho_{mn}(t)$ of a molecule driven by an external electric field using the TDHF approximation for the many-electron problem.[99,100]

$$\rho_{mn}(t) = \langle \Psi(t) | c_m^\dagger c_n | \Psi(t) \rangle \tag{1}$$

Here $|\Psi(t)\rangle$ is the many-electron wave function (time-dependent single-Slater determinant driven by an external field, where t is time), $c_m^\dagger$ (c_n) are creation (annihilation) operators, and the indices m and n refer to known basis functions (e.g., atomic orbitals, AOs, in the site representation). Within this theoretical framework, the changes induced in the density matrix by an external field are expressed as linear combinations of the electronic transition densities $\{\xi_\eta\}$[59,86] These are defined as:

$$(\xi_\eta)_{mn} = \langle \eta | c_m^\dagger c_n | g \rangle \tag{2}$$

and reflect the changes in the electronic density induced by an optical transition from the ground state $|g\rangle$ to an excited state $|\eta\rangle$. The transition densities (or electronic modes) are, in turn, the eigenfunctions of the two-particle Liouville operator L from the linearized TDHF equation of motion:[59,99–101]

$$L\xi_\eta = \Omega_\eta \xi_\eta \tag{3}$$

where the eigenvalues Ω_η are electronic $|g\rangle \rightarrow |\eta\rangle$ transition energies. The eigenvalue problem of Equation 3 may be written in the matrix form as:[59,99,102]

$$\begin{pmatrix} A & B \\ -B & -A \end{pmatrix} \begin{bmatrix} X \\ Y \end{bmatrix} = \Omega \begin{bmatrix} X \\ Y \end{bmatrix} \tag{4}$$

which is known as the first-order random phase approximation (RPA) eigenvalue equation.[59,101] The analogous eigenvalue problem is solved within an adiabatic TD-DFT framework.[72,78,92] Here X and Y are particle–hole and hole–particle

ADVANCED FUNCTIONAL MATERIALS

components of the transition density $\xi = \begin{bmatrix} X \\ Y \end{bmatrix}$ in the molecular orbital (MO) representation, respectively. The matrix A is Hermitian and identical to the configuration interaction (CI) singles matrix (CI singles is also known as the Tamm–Dancoff approximation), whereas the matrix B represents higher order electronic correlations included in the TDHF approximation and known as a de-excitation operator. The direct diagonalization of an operator L in Equation 4 is a potential computational bottleneck of the excited-state calculations. The CEO procedure circumvents this problem using numerically efficient Krylov space algorithms (e.g., Lanczos or Davidson).[59,92,103] This is possible since the action of the TDHF operator L on an arbitrary single electron matrix ξ can be calculated without constructing and storing the full matrix L in memory (so-called direct approach).[59,92,104] Subsequently, the computation of excited states is not substantially more numerically demanding than the ground-state calculations. The TDHF approximation accounts for essential electronic correlations, such as electron–hole interactions, including some additional higher order terms,[99,100,105] which are sufficient for a reasonably accurate calculation of UV-vis spectra in many extended organic molecular systems.[59] It has the advantage of being size-consistent in contrast to many truncated CI techniques.[97]

2.2. Exciton–Vibrational Dynamics and Relaxation

The vibrational dynamics after initial photoexcitation is followed using the ESMD approach,[85] which calculates classical nuclear trajectories on the excited-state adiabatic potential energy hypersurface. This initial photoexcitation (hot exciton) is allowed to evolve along the molecular excited-state potential energy surface $E_e(\mathbf{q})$ according to the Newtonian equations of motion for the nuclear degrees of freedom:

$$M_\alpha \frac{\partial^2 q_\alpha}{\partial t^2} + b\frac{\partial q_\alpha}{\partial t} = F_\alpha = -\frac{\partial E_e(\mathbf{q})}{\partial q_\alpha}, \quad \alpha = 1, ..., 3N-6 \tag{5}$$

using a numerical velocity Verlet finite difference algorithm.[106] Here q_α and M_α represent the coordinates and the mass, respectively, of one of the $3N$–6 vibrational normal modes (N being the total number of atoms in the molecule). The forces F_α are obtained as analytical derivatives of an excited-state energy $E_e(\mathbf{q})$ with respect to q_α.[93] We follow the dynamics of all ($3N$–6) nuclear degrees of freedom of the molecule. The excited-state potential energy surface $E_e(\mathbf{q})$ and the forces that enter into Equation 5 are quantum-mechanically calculated using the CEO method. Namely, for each nuclear configuration $\mathbf{q}$, $E_e(\mathbf{q}) = E_g(\mathbf{q}) + \Omega_\eta(\mathbf{q})$. The ground-state energy $E_g(\mathbf{q})$ and the vertical $|g\rangle \rightarrow |\eta\rangle$ transition frequency $\xi_\eta(\mathbf{q})$ are both calculated with the CEO technique.

The ESMD code makes it possible to follow picosecond excited-state dynamics of quite large (~1000 atoms) molecular systems taking into account all their $3N$–6 vibrational degrees of freedom. The simulations allow us to follow the gas-phase dynamics with vanishing damping ($b = 0$). In particular, by these means we can model coherent phonon dynamics in SWCNTs.[49] Imposing an effective viscous medium ($b \neq 0$) leads us to the excited-state optimal geometry, when the system is propagated sufficiently long for equilibration to occur. This allows us to study 'cold' exciton properties, such as self-trapping phenomena.[55] The excited-state vibrational relaxation is typically characterized by the dimensionless displacements Δ_α of each normal mode and respective Huang–Rhys factors $S_\alpha = \Delta_\alpha^2/2$. Geometry optimizations of a higher-lying excited state (e.g., the second exciton E_{22} of SWCNTs) becomes nearly impossible because of a significant density of states, level crossings, and the numerical expense involved. However, a rough approximation can be applied to estimate exciton–phonon effects. This assumes the same set of vibrational normal modes for both ground and excited states (neglecting Duchinski rotation and harmonic approximation). Subsequently, the gradient of the electronic transition energy $E_e(\mathbf{q})$ along the vibrational coordinate of interest q_α provides the exciton–phonon coupling element

$$V_\alpha^{ep} = \frac{\partial E_e(\mathbf{q})}{\partial q_\alpha} \tag{6}$$

and the approximate Huang–Rhys factor for an excited state of interest is given by:

$$S_\alpha = \frac{(V_\alpha^{ep})^2}{(\hbar\omega_\alpha)^2} \tag{7}$$

where ω_α is a frequency of the normal mode α. We previously found that such an approximation works well in the case of SWCNTs because of their rigid structure. Calculated displacements using 'exact' (optimal geometries) and 'approximate' (obtained by Eq. (7)) approaches for E_{11} agree within about 10 % for RBM for selected nanotubes, which translates to about 20 % differences in the Huang–Rhys factors.[67]

2.3. Real-Space Analysis

During the photoexcited dynamics, the molecular geometry gets distorted, and this, in turn, induces strong changes in the electronic wave function. To connect these structural changes with the distinct dynamics of the underlying photoinduced electron–hole pairs, we use a two-dimensional real-space analysis[59,86] of the calculated transition densities ξ_η (Eq. 2). The diagonal elements of the transition densities $(\xi_\eta)_{nn}$ represent the net charge induced in the n-th AO by an external field. The off-diagonal elements $(\xi_\eta)_{mn}$ $(m \neq n)$ represent the joint probability amplitude of finding an electron and a hole located on the m-th and n-th AOs, respectively. To obtain a two-dimensional real-space display of these modes, we coarse grain them over the various orbitals belonging to each atom. In practice, the hydrogens are omitted because they weakly participate in the delocalized electronic excitations. For other atoms, we use the following contraction: the total induced charge on each atom A is given by:

$$(\xi_\eta)_A = |\Sigma_{n_A}(\xi_\eta)_{n_A n_A}| \tag{8}$$

whereas an average over all of the off-diagonal matrix elements represents the effective electronic coherence between atoms A and B:

$$(\xi_\eta)_{AB} = \sqrt{\Sigma_{n_A m_B}\left[(\xi_\eta)_{n_A m_B}\right]^2} \quad (9)$$

Here the indices n_A and m_B run over all atomic orbitals localized on atoms A and B, respectively. The size of the resulting matrix $(\xi_\eta)_{AB}$ is now equal to $N' \times N'$, N' being the number of atoms in the molecule without hydrogens. Contour plots of $(\xi_\eta)_{AB}$ provide a real-space picture of electronic transitions by showing accompanying motions of optically induced charges and electronic coherence.[59,86] Two characteristic lengths are of relevance in these plots: The diagonal size of the non-zero matrix elements L_D reflects the degree of localization of the optical excitation (the position of the center of mass of the electron–hole pair). The largest off-diagonal extent of the non-zero matrix area (coherence length L_C) measures the maximal distance between the electron and hole (the exciton size). These L_D and L_C cross sections are shown later in Figure 5.

2.4. Simulation Details

The initial structures of fourteen SWCNTs of various length have been generated using TubeGen 3.3[107] and graphically visualized using XCrysDen software.[108] Unsaturated chemical bonds at the open tube ends (see Fig. 1) have been capped with hydrogen atoms and methylene (CH_2) groups to remove mid-gap states caused by dangling bonds. We have checked several different configurations of H- and CH_2-capping for each tube. Among these configurations, the final capping is accepted only if it provides a smooth dependence of the Hartree–Fock energy gap on the length of a SWCNT, approaching the limit of an infinite tube (simulated by imposing 1D periodic boundary conditions). Moreover, both finite-size and periodic-system approaches result in the nearly identical optimal geometries in the bulk of the tube (1–2 nm away from the tube ends). Subsequently, the tube ends do not introduce artefacts into tube geometries and their electronic structure. All simulated molecular systems have a finite length (varied from 1 to 10 nm) and comprise several repeat units (see Table 1). The maximum length of nanotubes is chosen to be significantly larger than the diameter of the tube and characteristic exciton sizes (about 5 nm, see below). If these conditions are satisfied, the finite-size 1D systems are expected to reproduce the properties of the infinite-size systems.

Furthermore, we used the MOPAC-2002 code[95] and AM1 model to obtain ground-state optimal geometries, heats of formation (chemical energies), and vibrational normal modes of all finite-size tubes (see Fig. 1). The vertical transition frequencies from the ground state to the singlet excited states, their oscillator strengths, and transition density matrices were then computed with the CEO procedure. The SWCNT singlet excitonic states E_{ii} formally correspond to van Hove singularities.[1] However, the ratio between excitonic energies violates predictions of conventional one-electron theories because of electronic correlation effects.[38] Excited states of the finite-size molecules are discreet in contrast to the band structure obtained from infinite tube calculations.[39,41,42] Each excitonic band is a manifold of closely spaced levels. The lowest state typically corresponds to the tightly bound exciton E_{ii}, which collects nearly all of the oscillator strength from its parent band. Conjugated polymers provide a well-explored example of such typical 1D electronic structures that share many striking similarities with the SWCNT case.[34,40,55,84]

The computed singlet states are strongly delocalized π–π excitations, which are optically accessible. Apart from the lowest

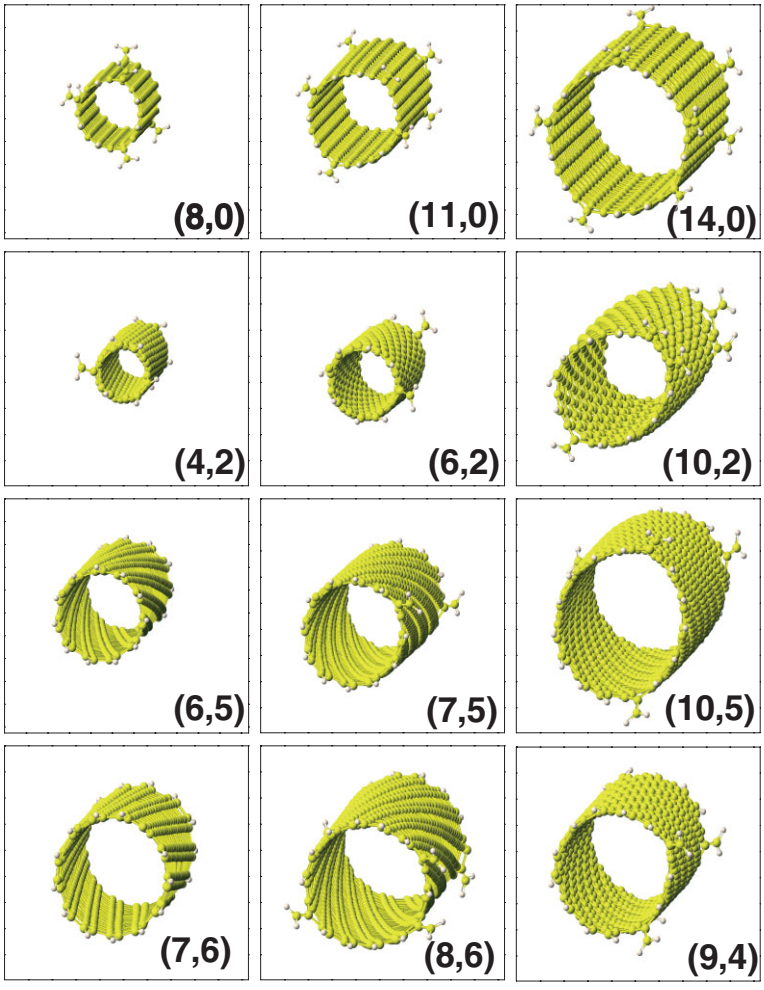

Figure 1. Optimal molecular structure of the carbon nanotubes considered in this work, presented in perspective depth view for visual comparison of tubes' diameters and chiralities. The upper row displays zigzag tubes, the lower rows present tubes with increasing chiralities. All tubes are finite and chosen to have approximately the same length: around 7–8 nm in the *Z*-direction. Electronic dangling bonds are terminated with either –H or –CH_2 capping agents.

Table 1. Calculated geometric parameters of carbon nanotubes.

Tube	Diameter [nm]	Unit length [nm]	Maximum number of units	Maximum length [nm]	Number of atoms
(4,2)	0.414	1.13	9	9.80	568
(6,2)	0.565	1.54	7	10.10	744
(8,0)	0.626	0.43	25	10.54	812
(6,5)	0.747	4.07	2	8.14	748
(7,5)	0.817	4.45	2	8.98	898
(11,0)	0.861	0.43	21	8.96	940
(10,2)	0.872	2.38	2	4.63	524
(7,6)	0.886	4.81	2	9.62	1040
(9,4)	0.903	4.92	1	4.86	562
(8,6)	0.952	2.59	3	7.82	920
(10,5)	1.039	1.13	7	7.79	1008
(14,0)	1.100	0.43	17	7.17	972
(16,0)	1.270	0.43	15	6.32	980
(19,0)	1.505	0.43	12	5.05	936

E_{11} excitation, the E_{22} excitation usually lies within the first 100 electronic states in all of the finite-size structures we considered. E_{11} and E_{22} calculations can be done routinely with the CEO procedure. In contrast, calculations of about 500–700 states are required to access the E_{33} excitonic band because of the high density of states in the high-frequency spectral region. This becomes numerically expensive and memory-demanding because the CEO computational effort typically scales linearly with the number of excited states requested.

To understand excited-state vibrational relaxation, we further optimized the geometry of the first optically allowed E_{11} excited state in the space of all vibrational coordinates **q** by using the ESMD approach, which is related to the nanotube emission properties. We also noted that there are several optically forbidden exciton states, nearly isoenergetic to the allowed E_{11} state in SWCNTs. The relative ordering of 'bright' and 'dark' states may be an intrinsic reason for the poor fluorescence efficiency of the CNTs.[40] We found that state ordering is highly method-dependent in semiempirical approaches. TD-DFT methodology was recently applied to address the state ordering, their delicate energetics, and optical activity.[109] The results agree well with experimental data and kinetic modeling.[109]

3. Results and Discussion

3.1. Heat of Formation and Energy Gaps

Figure 1 shows the structures corresponding to the minimum energy at the ground state for most types of SWCNTs studied and allows one to visualize tube sizes and chiralities. The geometric parameters of all calculated SWCNT species (ten chiral and five zigzag tubes) are given in Table 1. Tthe heat of formation per carbon atom for the fourteen SWCNTs at their maximum length (calculated with the MOPAC-2002 code[95]) is presented in Figure 2. The heat of formation is a standard enthalpy of formation or the enthalpy change to form a mole of molecular compound at 25 °C from its elements. Figure 2

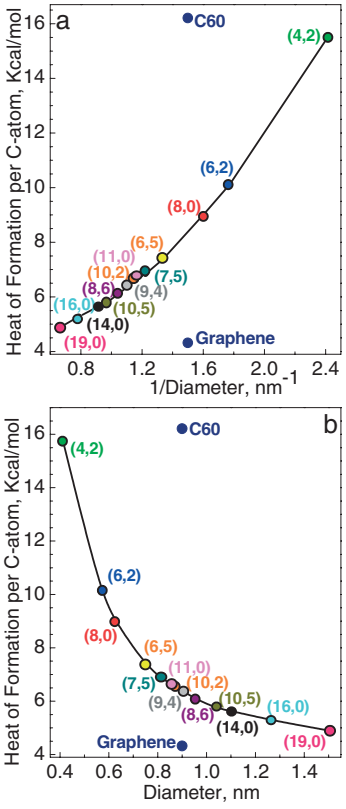

Figure 2. Variation of calculated heat of formation per carbon atom as a function of a) inverse tube diameter and b) tube diameter, *D*. Wider tubes have the lower heat of formation and are more frequently observed in experiments. For comparison, calculated heats of formation for fullerene C60 ($D = 0.71$ nm) and graphene are shown as well.

shows that tubes with smaller diameters (~0.5 nm), and, consequently, larger curvatures, have much larger heats of formation than wider tubes. The aromatic rings in nanotubes are no longer planar but distorted due to curvature. This leads to deviation from the energetically preferable ideal sp^2 hybridization and π-delocalization of the graphene sheet. The curve in Figure 2

becomes flater for tubes with diameters of about 1 nm, which is a common size of SWCNTs used in experiments. Such a strong difference in the heat of formation between small and large SWCNTs explains the fact that very narrow tubes are much harder to synthesize and are rarely observed in experiments.[110] Tube-geometry deformation related to the curvature leads to a number of electronic phenomena, such as Peierls distortion and gap opening in metallic tubes.[1,54,69–71] Below we discuss these geometric effects on the excitonic structure of semiconducting SWCNTs.[49,55]

The one-electron uncorrelated AM1/HF energy gap (the energy difference between the lowest unoccupied molecular orbital (LUMO) and the highest occupied molecular orbital (HOMO)) is shown in Figure 3a and c. The respective calculated correlated CEO gaps are displayed in Figure 3b and d. Figure 3a demonstrates the effects of the finite length of the

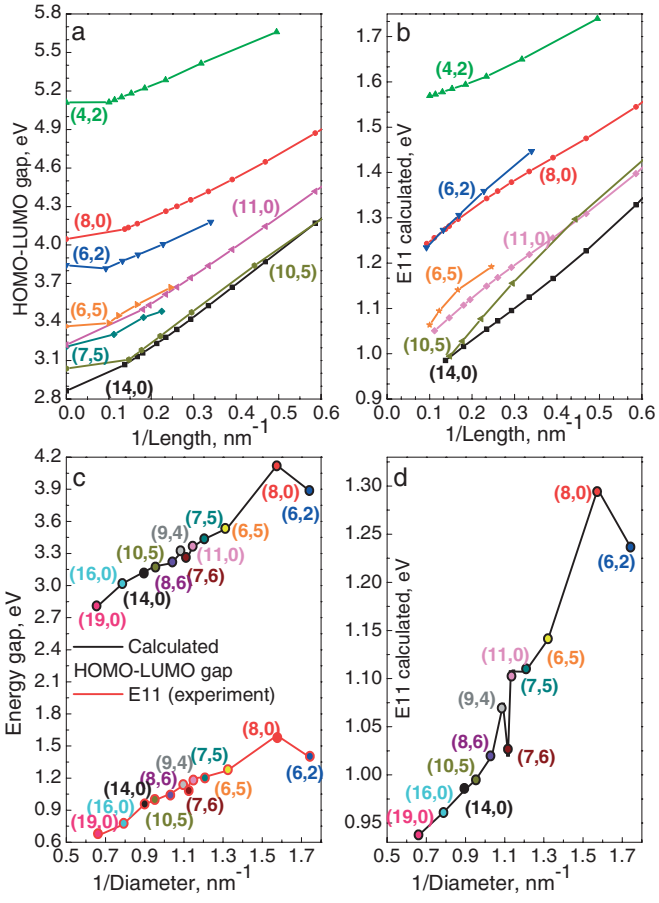

Figure 3. Energy of the first optical transition (E_{11}) of various tubes as a function of a,b) inverse tube length, and c,d) inverse tube diameter. Panels (a) and (c) show the scaling of the uncorrelated HF/AM1 energy gap (HOMO–LUMO). Panels (b) and (d) show scaling of the E_{11} transition energy obtained with the CEO (TDHF/AM1) method, which incorporates essential electron–hole interactions (excitonic effects). Experimental data for the first optical transition from the literature [22, 23] are given by the red line in (c) for comparison. Overall, the calculated energy gaps reproduce trends seen in measured energies well. The HF/AM1 level overestimates experimental values by nearly 2 eV, which is attributed to the lack of electronic correlations. The CEO results coincide well with experimental data with an accuracy of about 10–15 %.

SWCNTs studied on their electronic structures. The smooth dependence of the energy gap on the reciprocals of the tube length, roughly following a $1/L$ scaling law, assumes that the terminated tube ends have saturated dangling bonds and do not introduce their own electronic states to the tube gap even in very short tubes. This can also be directly confirmed by plotting the relevant HOMOs and LUMOs (not shown). Subsequently, the energy gap of the capped finite SWCNTs asymptotically approach the infinite tube limit (Fig. 3a).

The dependence of the calculated HF energy gaps on a tube diameter and its comparison with experimental data are shown in Figure 3c. For uniform comparison, all calculated values are shown for tubes with roughly the same length (6.5–7 nm). The calculated dependence demonstrates a surprisingly good agreement with experimental results. Mod-1 and mod-2 tube families (defined as mod(n–m,3) = 1 or 2, respectively, are clearly distinguished by red-shifted energies of mod-2 tubes (7,6) and (6,2). Thus, the qualitative behavior of both calculated and experimental energies versus tube diameter strongly coincide. However, calculated HF energy gaps are uniformly shifted up by about 2 eV compared to the experimental values for all considered SWCNTs. The over-estimation of the energy gap is a common feature of the HF calculations and can be corrected by the inclusion of electronic correlations (i.e., Coulomb interaction between excited electrons and holes). Calculated with the CEO, correlated E_{11} optical transition energies at the TDHF/AM1 level are red-shifted by nearly 2 eV compared to the respective HF values; however, all scaling trends are preserved, as illustrated in Figure 3b and d. Compared to the corresponding experimental data, the CEO results exhibit a red-shift up to 0.15 eV for the tubes with a diameter less than 1 nm. This red-shift originates from the AM1 Hamiltonian, which also often underestimates energy gaps for polymers.[96] In contrast, the tubes with diameters larger than 1 nm that were considered show small blue-shifts of transition energies from experimental values. This deviation grows with tube diameter because the characteristic excitonic sizes enlarge with diameter increase (see discussions below). Subsequently, the tube end effects start to introduce quantum confinement along the tube in the widest tubes (16,0), and (19,0), where computations are limited to relatively short segments (~7 nm in length).

Finally, we discuss emerging size-scaling laws for calculated energy gaps. There has been substantial effort in carbon-nanotube research to develop scaling relationships between tube diameter and excitation energy (commonly used for Kataura plots) well beyond the simple $1/D$ dependence. Modern empirical scaling laws accurately reproduce experimental data for a broad range of tube diameters and account for chirality effects.[23,47,94] Similar work was done in the conjugated-polymer field to extrapolate the scaling of bandgap energies of finite oligomers to the polymer limit.[82,83] However, an inverse approximate relationship $1/L$ between an energy and a length, which may be rationalized with a free-electron model,[111] does not recover a finite bandgap at infinite length. Indeed in Figure 3a, we observe that calculated energy gaps of the infinite-length SWCNTs demonstrate saturation effects as the gap be-

comes roughly constant at some large length. Instead of $1/L$ dependence, more sophisticated relationships based on the interacting oscillator models were introduced by Kuhn and applied to organic dyes.[111–113] This approach was later extended within an exciton formalism.[114,115] In particular, the following scaling relationship has been successfully used for conjugated-polymer fitting in a recent review:[83]

$$\Delta E = A\sqrt{1 + B\cos\left(\frac{\pi}{N+1}\right)} \tag{10}$$

Here N is the number of repeat units in the segment, and A and B are fitting constants. We use Equation 10 to fit both calculated uncorrelated and correlated gaps of narrow (4,2) and relatively wide (14,0) tubes. The results, presented in Figure 4, show a good fit for E_{11} gaps in short and long segments, as well as the infinite tube limits, and clearly demonstrate deviation from the $1/N$ relationship at long tube lengths.

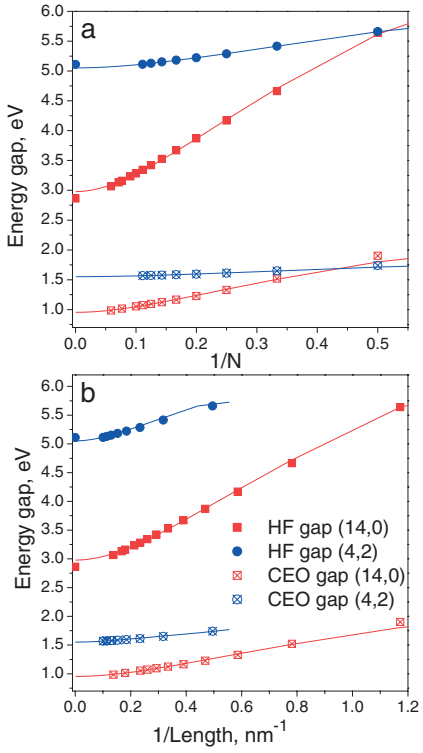

Figure 4. Kuhn fit of the calculated uncorrelated and correlated energy gaps of (14,0) and (4,2) finite tubes using Equation 10 as a function of a) an inverse number of repeat units and b) an inverse tube length. Deviation from $1/N$ ($1/L$) relationship at long tube lengths is clearly seen.

3.2. Structure of Excitons

To study the E_{11} and E_{22} exciton structures, we calculate up to 100 lowest singlet excited states for each SWCNT from Table 1 at the ground-state (GS) optimal geometry. E_{11} and E_{22} states have characteristically strong oscillator strength, which results in distinct peaks in the SWCNT's linear absorption spectra probed by a variety of spectroscopic techniques.[22,29–34] The contour plots presented in the first and second column in Figure 5 represent the transition density matrices between the ground and electronically excited E_{11} and E_{22} levels, respectively. These plots can be considered as 'topographic' maps that reflect how the single-electron reduced density matrix changes upon molecular photoexcitation, as described in Section 2.3.[59] In all color panels the axes correspond to carbon atoms, whose coordinates are labeled along the tube axis. Subsequently, these plots mostly reflect the distribution of the excitonic wave function along the tube. In principle, transition density matrices contain the radial distribution

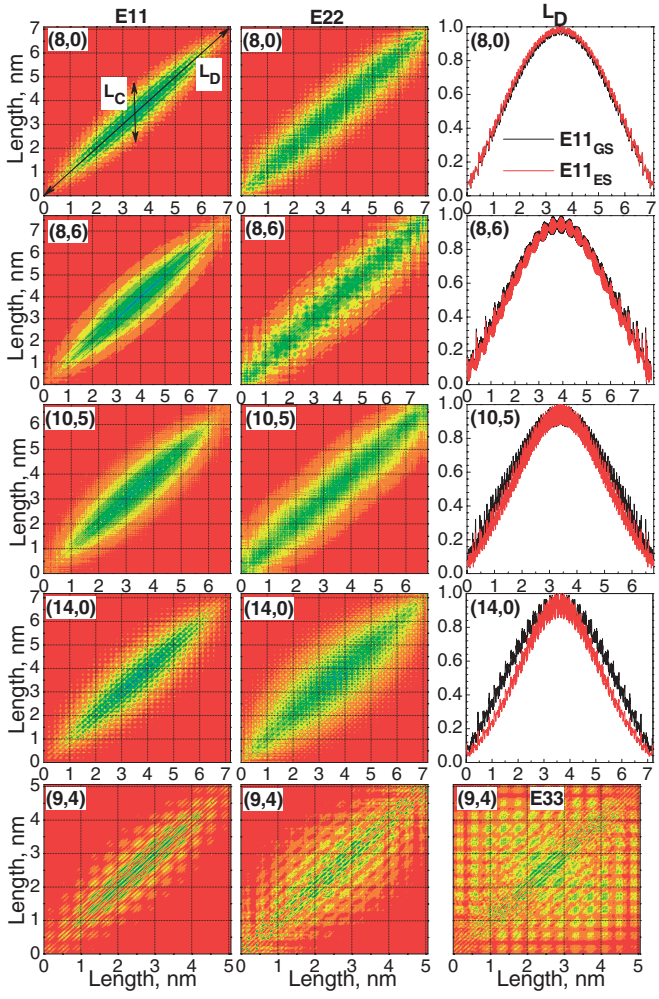

Figure 5. Comparison of the first (E_{11}) and second (E_{22}) excitonic transition densities at ground state (GS) and the lowest optically excited-state (ES) optimal geometries for various tubes. The first and second columns display two-dimensional contour plots of transition density matrices for E_{11} and E_{22} excitons, respectively, as a function of electron (*Y*-axis, nm) and hole (*X*-axis, nm) coordinates at GS geometry. The bottom row also shows the third excitonic transition (E_{33}) calculated for a (9,4) tube, corresponding to delocalized excitation. Transition density magnitude scales from red (0) to violet (1) through the natural rainbow color sequence. The third column shows the diagonal slice (L_D) of the E_{11} transition density matrix as a function of electron–hole pair position along a tube. Black and red lines correspond to GS and ES geometries, respectively. Tubes with larger diameter exhibit higher localization of the E_{11} exciton in the middle of a tube (self-trapping) at ES geometries compared to the GS profile.

of the excitonic wave function as well; however, these properties can not be visualized from the 2D color maps in Figure 5, which reflect a rather averaged description.

The matrix diagonal elements (L_D direction) characterize the distribution of an excitonic wave function over the length of the tube. The relevant cross sections along the diagonal L_D are shown in the right column in Figure 5, which compares localization of the exciton at the ground and excited-state geometries. Figure 5 demonstrates that the center of mass of E_{11} and E_{22} excitons is spread over the entire tube for all studied SWCNTs. The amplitudes vanish at the tube ends, which reflects excitonic scattering (reflection) at the ends.[60] Such exciton delocalization patterns are identical to that observed in conjugated polymers.[55,59,85] There are a few other similarities between excitonic features in these molecular systems. For example, L_D plots for all studied tubes have periodically repeating peaks in the electronic density due to photoexcitation. The chiralities of SWCNTs determine the shape and the period of these peaks. These periodic variations are a signature of the spontaneous weak dimerization of the π electronic density.[55] Such effects are especially pronounced in the conjugated-polymer case.[85] The dimerization is very weak in the narrow tubes (e.g., (8,0)) because of bonding strain and disruption of π-conjugation induced by the tube curvature. The peak amplitudes increase in the medium-diameter tubes (e.g., (14,0)), reflecting enhanced mobility of π electronic systems. However, subsequent reduction is expected because of smaller π–σ mixing and vanishing Peierls dimerization in super-wide SWCNTs and planar graphene sheets.[1] These electronic phenomena have clear vibrational signatures as well and lead to Peierls distortion, which will be discussed in the next subsection.

Another important characteristic of the electronic excitation is the exciton coherence size (maximal distance between electron and hole) given by the largest off-diagonal extent (L_C) of the non-zero matrix area. The L_C cross section of the transition density (Fig. 5) represents the probability distribution of an electron coordinate, when the position of a hole is fixed in the middle of a tube surface. Such representation is typically used to describe excitonic delocalization.[39,94] Contour plots in Figure 5 show that L_C is finite for both E_{11} and E_{22} excitations for all tubes. This corresponds to the tightly bound singlet excitons, with L_C being 3–5 nm (depending on the tube diameter, see discussion below). Other excitons are present in SWCNTs as well. For example, triplet excitations recently calculated by the TD-DFT approach[84] are even stronger bound excitons with an L_C size of about 1 nm; these excitaitons are 0.2–0.3 eV below their singlet counterparts. Different types of singlet excitations, appearing in the nonlinear[30,34] and two-photon[32,33] absorption region for SWCNTs, are weakly bound excitons.[34,84] Such excitations are typical and have been extensively studied in many other 1D materials, such as conjugated polymers.[34,59,83,85] The E_{33} state calculated for the (9,4) tube (bottom right panel in Fig. 5) is nearly uniformly delocalized over the entire tube, with an L_C size comparable to the tube length. This corresponds to either an unbound or weakly bound excitonic state.[94] The interpretation of E_{33} being a delocalized excitation, unlike bound E_{11} and E_{22} states, agrees with experimental results and shows that E_{33} and E_{44} optical transitions exhibit different diameter scaling compared to that of E_{11} and E_{22}.[94] However, this contradicts the previous theoretical studies based on the *GW* approximation,[39] where E_{11}, E_{22}, and E_{33} levels are all tightly bound excitons. Such a discrepancy may point to important electronic structural features of SWCNTs, such as mixing and various non-Condon interactions between E_{33} states and the continuum of the lower lying E_{11} and E_{22} bands. Our calculations estimate less than 0.001 eV separation in the density of states at the E_{33} level, attributed to other molecular states, compared to about 0.02 eV separation at the E_{22} level. Subsequently any small perturbation (e.g., temperature or dielectric inhomogeneity and disorder) may result in interactions and superpositions of delocalized and localized states in experimental samples. In finite tube calculations these perturbations come naturally from the end effects and imperfect optimal geometries, whereas the wavevector $\boldsymbol{k}$ allows for separation of 'pure' excitonic bands in the calculations with imposed periodic boundary conditions. We note that such non-Condon phenomena were recently observed at E_{22} level in SWCNTs.[31,66,67]

Finally we discuss scaling of the exciton size L_C with the tube diameter. A recent study, which utilized a tight-binding method parameterized by ab initio (*GW*/LDA) results, proposes a simple scaling relation for L_C, having a leading dependence on diameter D with chirality corrections.[116] These calculations define exciton sizes as a Gaussian width of the exciton wave function $|\psi|^2$ along the tube axis, and obtain the L_C extent of E_{11} in the range of 1–2 nm.[116] In another model calculation, the exciton size L_C was prescribed to the root mean square (rms) distance between electron and hole.[41] Obviously L_C can be quite arbitrary and subjectively defined as the exciton wave function span along the tube axis. We suggest that a more practical definition of L_C, in conjunction with experimental conditions, should include the 'full' extent of the wave function. We recall that in other 1D systems, such as conjugated polymers, a saturation of physical observables (e.g., transition energies and polarizabilities) is developed when the system becomes larger than the exciton size L_C. This constitutes the fundamental transition from quantum confinement to 'bulk' regime,[59,81,83,117] which occurs well beyond L_C sizes defined as the half-width of the distribution. In our simulations we fitted the L_C cross section of the E_{11} transition density matrices (Fig. 5), which corresponds to the excitonic wave function $|\psi|^2$ along the tube axis, by a Lorentzian function (an example of the fit is shown in the inset in Fig. 6). The L_C exciton size is further approximated by the width of a Lorentzian function at one tenth of its maximum amplitude. The resulting dependence of calculated L_C on the tube diameter (Fig. 6) spans a 2–5 nm range. Overall the curve roughly follows the previously observed $\sim D$ dependence (due to better π-electron conjugation in wider SWCNTs), except for the very narrow (4,2) tube. Our absolute L_C magnitudes significantly overestimate previous calculations,[116] because of the different definitions discussed above, but correlate well with commonly accepted values of about 2–3 nm determined for conjugated polymers.[81,83] The vibrational relaxation leading to ES geometries (discussed in the next subsection) results in a

ADVANCED FUNCTIONAL MATERIALS

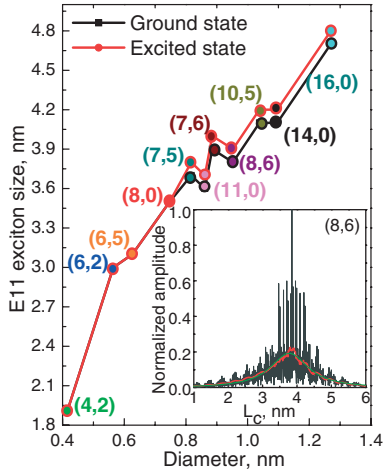

Figure 6. Comparison of calculated E_{11} exciton size at GS (black line) and ES (red line) geometries for various tubes. The inset shows an example of the L_C slice of the transition density matrix of an (8,6) tube as a function of electron coordinate, when the hole is fixed in the middle of a tube (black line). The red line stands for the averaged transition density over the radius; the green line shows the corresponding Lorentzian fitting. The exciton size (maximal distance between an electron and a hole) is defined as the width of the Lorentzian fit at 0.1 of its height, which approximately corresponds to a 90% drop of the excitonic wave function. The size of an exciton increases with tube diameter. The exciton size is slightly larger at the ES geometry for wide tubes, where vibrational relaxation leads to the smoother surface.

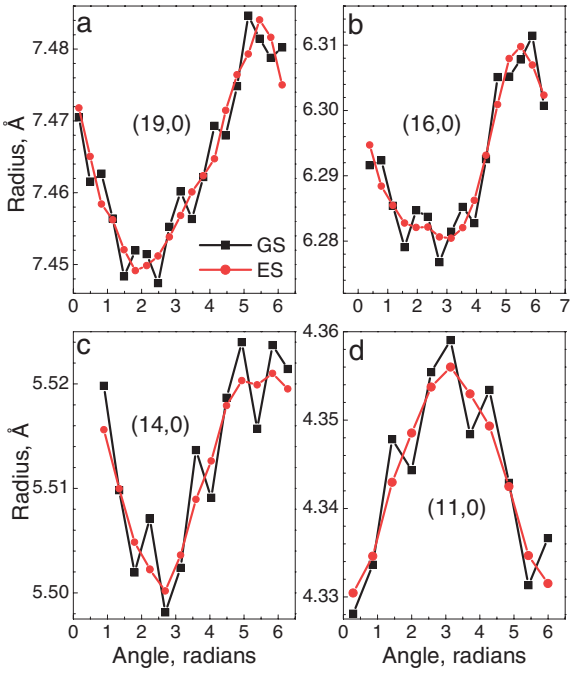

Figure 7. Variation of tube radius as a function of azimuthal angle for GS (squares, black line) and ES (circles, red line) geometries of various zigzag tubes. The GS geometry is corrugated for all considered tubes, while the ES geometry exhibits a smoother surface shape and, thus, decreased Peierls distortion.

slight increase of the exciton size in large tubes (compare black and red lines in Fig. 6). In narrow tubes, this effect disappears and the exciton size stays almost unchanged upon relaxation of the photoexcitation.

3.3. Photoexcited Vibronic Dynamics and Relaxation

As expected, electron–phonon coupling leads to different optimal geometries of ground and excited states. Figure 7 shows a comparison of GS and ES structures calculated for zigzag nanotubes by presenting the changes of a tube radius versus its azimuthal angle. Each data point in Figure 7 corresponds to the position of a carbon atom along a cross section perpendicular to the tube axis and taken in the middle of a tube to reduce possible edge effects of finite SWCNTs. For all studied zigzag tubes, we observe two main maxima and minima in the radius dependence on the angle. This indicates a slightly elliptical shape of the cross section for both GS and ES geometries, deviating from a perfect cylindrical geometry. We also note that chiral SWCNTs do not show such elliptical aberrations at both GS and ES geometries (not shown). An important feature of the GS geometry is the corrugation of the tube surface,[55] which appears as sharp peaks in the radial dependence in Figure 7. Such surface corrugation in the GS geometry obviously makes some bonds shorter and some bonds longer in the hexagonal cell, which, in turn, reflects the related variations of the electronic density shown in the right column in Figure 5. Similar to zigzag tubes, chiral SWCNTs also have a distorted GS geometry.[55] Because of the rigid structure, the respective nanotube bond-length alternation is about 0.01–0.02 Å, which is at least ten times smaller than that in conjugated polymers. This geometric distortion, caused by interactions of the π–σ-electron system because of curvature, has many common features with the effect of spontaneous symmetry breaking, also known as Peierls distortion. The latter phenomenon is attributed to the instability of the Fermi energy states in quasi-one-dimensional metals. In half-filled-zone materials, the instability is removed by electron–phonon interactions, leading to gap opening at the Fermi level (metal–semiconductor transition) and induced by the folding of the Brillouin zone and related doubling of the real-space lattice period.[118] Conjugated polymers provide an example of such a transition, with a gap opening of about 2 eV.[58] Peierls distortion has been extensively studied in metallic nanotubes.[1,54,70,119–121] In contrast to polymers, the produced bandgap in metallic nanotubes is smaller than the energy of thermal fluctuations. In a previous study,[55] we considered semiconductor SWCNTs and found that their surface experiences corrugation, fully analogous to the lattice period doubling. As this spontaneous symmetry breaking is associated with the electron–phonon interaction, we refer to it as Peierls distortion. However, this phenomenon cannot be considered as a metal–semiconductor transition.

In the ES geometry, the nanotube surface becomes locally less distorted. That is reflected by a smoother radial dependence on the angle (red lines in Fig. 7). Figure 8 shows the difference between the radial distance of carbon atoms along the tube length in the ground and excited geometries for both zigzag and chiral SWCNTs. The periodic oscillations reflect the decrease of Peierls distortions upon relaxation of photoexcita-

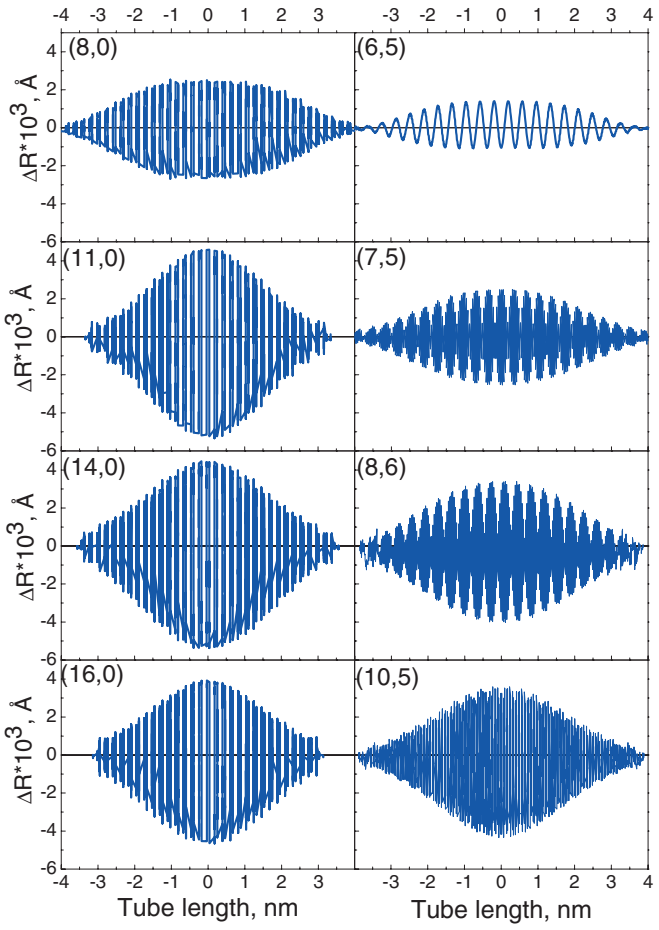

Figure 8. Change of the radius $\Delta R = R_{ES} - R_{GS}$ with carbon coordinate along the tube *Z*-axis for various tubes. Chiral and zigzag tubes are shown in the first and second columns, respectively. Tube diameters increase from the top panels to the bottom ones. Wider tubes have a larger difference between GS and ES geometries because of substantial excitonic relaxation, which leads to self-trapping of the exciton (shown in Fig. 5).

tion. The largest geometric changes develop in the middle of the tubes. Overall, zigzag tubes show larger structural relaxation in the ES than chiral SWCNTs (compare left and right columns Fig. 8) in agreement with previous work.[28] This vibrational relaxation vanishes in the limit of very narrow tubes[55] because of disruption of π-conjugation and curvature-induced strain. The radial difference in Figure 8 shows that vibronic relaxation increases and reaches a maximum for tubes with diameters of about 1 nm. For tubes that are wider than 1 nm, the radial difference becomes smaller (compare (16,0) and (14,0) tubes in Fig. 8) and approaches zero in the limit of infinitely wide tubes. This shows the vanishing effect of tube curvature, leading to the GS geometry distortion and related excited-state vibronic relaxation.

The average diameter change upon E_{11} exciton relaxation leads either to slight tube buckling, mostly for the mod-1 tube family, or narrowing, for mod-2 tubes. This situation inverses for the E_{22} exciton case.[28,94] The average diameter change is, however, small compared to the bond-length changes.[55] Subsequently, the RBM has smaller electron–phonon coupling compared to that of the longitudinal G-mode. Typical calculated dimensionless displacements along the E_{11} potential energy surface for RBM and G-modes are 0.1–0.15 and 0.3–0.6, respectively, for SWCNTs with a diameter of approximately 1 nm (detailed studies of which have been published recently[49,66,67]). Such values correspond to a weak electron–phonon coupling regime compared to most molecular materials. Nevertheless, local distortions of the tube surface during vibronic relaxation (Fig. 8) lead to experimentally detectable coherent phonon dynamics and anharmonic coupling between the RBM and G-mode, which appears in the excited-state potential.[49]

The lattice distortions in the middle of the tube (Fig. 8) result in the localization of the E_{11} exciton in the center of the molecule (compare black and red lines in the right column in Fig. 5), known as exciton self trapping in SWCNTs[55] and conjugated polymers.[85] This can be clearly seen in both chiral[55] and, in particular, zigzag tubes with diameters around 1 nm (e.g., (14,0) demonstrate the largest excitonic localization near the center, as shown in Fig. 8). Subsequently, the related diagonal L_D size reduces upon vibrational cooling. In contrast, because of a smoother potential in the absence of Peierls distortions, the L_C size slightly increases in the ES geometries (Fig. 6).

To characterize the effects of electron–phonon coupling on the electronic degrees of freedom, we further analyze the Stokes shift (defined as a difference between vertical transition energies at GS and ES geometries) and the energy change of the E_{11} excited state upon vibrational relaxation. Figures 9 and 10 show calculated values of these quantities as a function of tube length and diameter, respectively. The greater the ES geometries deviate from the equilibrium GS structure, the stronger the energy changes are, as observed in Figures 9 and 10. The shorter tubes exhibit stronger vibrational relaxation effects (Fig. 9). This is expected because molecular systems in a quantum confinement regime usually undergo larger change of the wave function upon electronic excitation, and, subsequently, stronger vibronic effects (such trends in conjugated oligomers were explored in the literature[85]). When tubes are much longer than the corresponding exciton size L_C, both Stokes shift and vibrational relaxation energies show noticeable convergence to a relatively low value, comparable with thermal energy. Both quantities converge roughly as $1/L$ with deviations at large tube lengths. Such convergence is similar to what we observe for energy gap scaling (Fig. 3), and usage of fitting formulae, like Equation 10, may be necessary for extrapolation to the limiting values. Unfortunately, excited-state relaxation in long tubes wider than 1 nm diameter was not calculated because of the large numerical expense of the deployed method.

Unlike generally observed $1/L$ or $1/D$ trends, the dependence of the Stokes shift and vibrational relaxation on tube diameter, as presented in Figure 10, is strongly nonlinear. Such dependence matches the above-mentioned concept of diameter-dependent rigidity. The narrowest tube (4,2), with a diameter comparable to the phenyl ring size, does not show any vibrational effects caused by disrupted π-conjugation and consider-

ADVANCED FUNCTIONAL MATERIALS

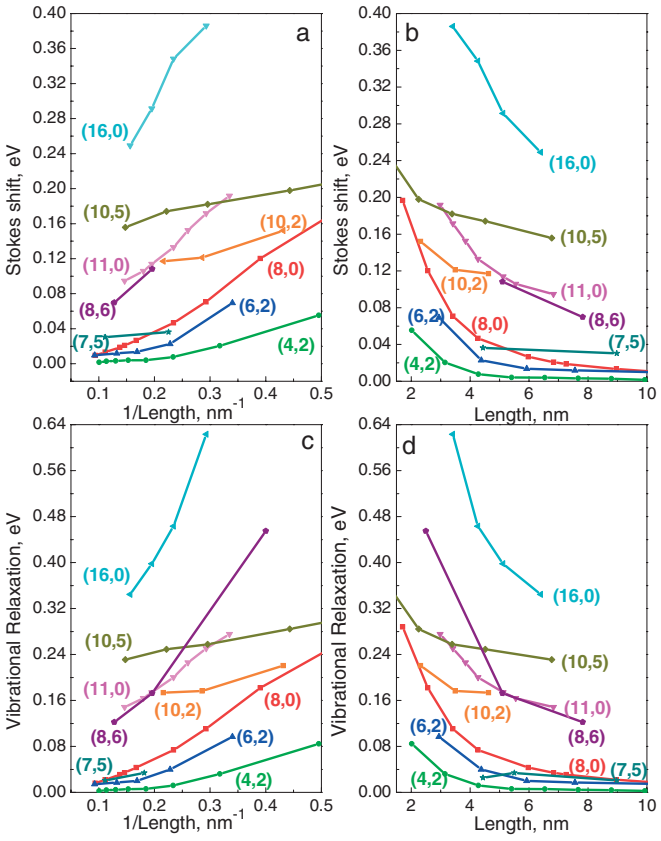

Figure 9. Variation of calculated electron–phonon coupling with a,c) inverse tube length and b,d) tube length. The Stokes shift and excited-state vibrational relaxation are shown in panels (a,b) and (c,d), respectively.

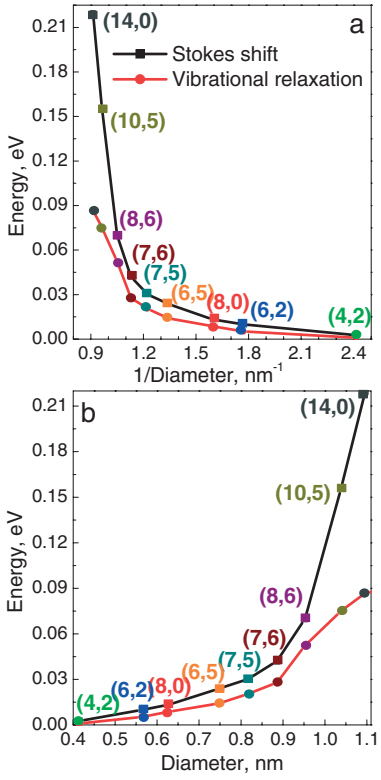

Figure 10. Variation of calculated Stokes shift and excited-state vibrational relaxation as a function of a) inverse tube diameter and b) tube diameter.

able bonding system strain, which does not allow carbon atoms to move upon optical excitation. Slightly larger tubes, such as (6,2), (8,0), and (6,5), have very small relaxations. Tubes with diameters of about 1 nm are less rigid, have better π-electron mobility, and, consequently, show 50–200 meV Stokes shifts and 30–90 meV excited-state relaxation. Such effects are detectable in the absorption/emission profiles of SWCNTs. In particular, even though the main transition in the spectra corresponds to the 0–0 line, weak vibrational replica (particularly G-mode) are clearly seen,[43,44] which amounts to the 'spectral weight transfer' of about 10 % to electron–phonon lines.[45,46,53,55]

Finally, we note that Stokes shifts are usually defined in experiments as the spectral shift between absorption and emission maxima. In molecular systems with large vibrational coupling and displacements this roughly coincides with the difference between the vertical transition energies at GS and ES geometries, which is identical to the computational definition of Stokes shift. Comparison of experimental and calculated Stokes shifts in SWCNTs is, however, not straightforward. Because of relatively small vibrational effects, the main transition in the spectra of SWCNTs corresponds to the 0–0 line; consequently, very small shifts are observed between the maxima of absorption and emission profiles. These shifts in the 0–0 line are related to the environmental relaxation and possible exciton transport along the tube. However, these quantities do not reflect the internal vibrational relaxation of the tube, which is the origin of fairly substantial computed Stokes shifts (see Figs. 9 and 10). Subsequently, to compare calculations and experimental measurements, shifts of the center of mass of absorption and emission profiles (including complete vibrational progressions) need to be evaluated. These should provide experimental estimates and comparisons of internal vibrational relaxation and environmental relaxation in SWCNTs. This will be the subject of future studies.

4. Conclusions

Investigations of the electronic structure and spectroscopic properties of SWCNTs are of primary importance for successful development of novel electronic and photonic devices based on SWCNTs, as well as for ongoing global progress in nanoscience and nanotechnology. The recent realization of the significance of electron–electron interactions and electron–phonon coupling in SWCNTs immediately emphasized the usefulness of modern numerically expensive quantum-chemical calculations,[39,42] compared to model-type analytical approaches.[1] In addition to the solid-state-based approaches that assume homogeneous/ordered infinite SWCNTs,[39–42] finite-size calculations have addressed many important aspects of nanotube photophysics.[34,40,49,55,80,84] The latter approach is legiti-

mate if the lengths of the considered tube segments are larger than the corresponding diameter and the exciton size L_C.

Our reported ESMD simulations of finite SWCNTs provide important details of photoinduced dynamics, which were not accessible previously. In addition to the optimal geometries and single-point electronic structure, which are available from traditional simulations, our approach directly explores excited-state vibrational relaxation and exciton–phonon coupling, accounting for curvature effects and related σ–π interactions. Good agreement with experimental data is achieved for energies of excitonic transitions (e.g., Fig. 3 and the literature[55]), electron–phonon coupling constants,[67] and time-resolved experimental data.[49] The fundamental effects, such as tightly bound and unbound excitons,[94] Peierls-like distortions,[55] and exciton self-trapping,[55, 122] are found to be important features of the excited-state structure in SWCNTs. Substantial excited-state displacements and Huang–Rhys factors[66,67] computed in the tubes with ~1 nm diameter result in the noticeable Stokes shifts and vibrational relaxation energies, which can be examined experimentally.[66,67] Our calculations quantitatively explore the scaling dependence of excitonic and vibrational properties of SWCNTs on their diameters, lengths, and chiralities. In particular, the explored length dependence, besides being a tool for extrapolating data to the limiting values, may have broader physical content.

Solid-state approaches, assuming uniform infinite tube lengths, characterize excitons that have a coherence length L_C, that is, by spatial separation between photoexcited electron and hole. Molecular-type finite-size calculations necessarily introduce the L_D size, which is related to the position of the center of mass of the exciton along the tube. On the ideal infinite tubes, of course, this quantity should have a trivial uniform distribution. However, in the experimental samples the tubes are subject to a dielectric environment, solvent-induced disorder, local defects, chemical functionalizations, intertube interactions, and so on. All these effects can lead to the spatial localization of the exciton (e.g., Anderson-type localization). Such phenomena are difficult to model using the infinite-tube approach with imposed periodic boundary conditions. In contrast, all these perturbations and inhomogeneities are routinely accessible within molecular approaches dealing with finite-tube segments.

Intelligent manipulation of nanotube ensembles and their assembly into functional devices, which make use of the emergent properties of the SWCNTs, are aims of current technological and synthetic work. Understanding the role of possible defects, disorder effects, and intertube interactions present theoretical challenges, where the molecular-type approaches could make significant contributions in future studies.

Received: March 16, 2007
Revised: June 22, 2007
Published online: October 4, 2007

[1] R. Saito, G. Dresselhaus, M. S. Dresselhaus, *Physical Properties of Carbon Nanotubes*, Imperial College Press, London, UK **1998**.
[2] M. S. Dresselhaus, G. Dresselhaus, P. Avouris, *Carbon Nanotubes: Synthesis, Structure, Properties, and Applications*, Springer, Berlin **2001**.
[3] M. Terrones, *Int. Mat. Rev.* **2004**, *49*, 325.
[4] J. Kong, N. R. Franklin, C. Zhou, M. G. Chapline, S. Peng, K. Cho, H. Dai, *Science* **2000**, *287*, 622.
[5] E. S. Snow, F. K. Perkins, E. J. Houser, S. C. Badescu, T. L. Reinecke, *Science* **2005**, *307*, 1942.
[6] B. C. Regan, S. Aloni, R. O. Ritchie, U. Dahmen, A. Zettl, *Nature* **2004**, *428*, 924.
[7] N. Mason, M. J. Biercuk, C. M. Marcus, *Science* **2004**, *303*, 655.
[8] M. J. Biercuk, N. Mason, C. M. Marcus, *Nano Lett.* **2004**, *4*, 1.
[9] M. S. Dresselhaus, *Nature* **2004**, *432*, 959.
[10] Y. C. Chen, N. R. Raravikar, L. S. Schadler, P. M. Ajayan, Y. P. Zhao, T. M. Lu, G. C. Wang, X. C. Zhang, *Appl. Phys. Lett.* **2002**, *81*, 975.
[11] K. Terabe, T. Hasegawa, T. Nakayama, M. Aono, *Nature* **2005**, *433*, 47.
[12] S. Y. Set, H. Yaguchi, Y. Tanaka, M. Jablonski, *J. Lightwave Tech.* **2004**, *22*, 51.
[13] S. Y. Set, H. Yaguchi, Y. Tanaka, M. Jablonski, *IEEE J. Sel. Top. Quant. Electron.* **2004**, *10*, 137.
[14] J. A. Misewich, R. Martel, P. Avouris, J. C. Tsang, S. Heinze, J. Tersoff, *Science* **2003**, *300*, 783.
[15] H. W. C. Postma, T. Teepen, Z. Yao, M. Grifoni, C. Dekker, *Science* **2001**, *293*, 76.
[16] Z. H. Chen, J. Appenzeller, Y. M. Lin, J. Sippel-Oakley, A. G. Rinzler, J. Y. Tang, S. J. Wind, P. M. Solomon, P. Avouris, *Science* **2006**, *311*, 1735.
[17] D. Chattopadhyay, L. Galeska, F. Papadimitrakopoulos, *J. Am. Chem. Soc.* **2003**, *125*, 3370.
[18] R. Krupke, F. Hennrich, H. von Lohneysen, M. M. Kappes, *Science* **2003**, *301*, 344.
[19] Z. Chen, X. Du, M.-H. Du, C. D. Rancken, H.-P. Cheng, A. G. Rinzler, *Nano Lett.* **2003**, *3*, 1245.
[20] M. J. O'Connell, E. E. Eibergen, S. K. Doorn, *Nat. Mat.* **2005**, *4*, 412.
[21] M. Zheng, A. Jagota, M. S. Strano, A. P. Santos, P. Barone, S. G. Chou, B. A. Diner, M. S. Dresselhaus, R. S. McLean, G. B. Onoa, G. G. Samsonidze, E. D. Semke, M. Usrey, D. J. Walls, *Science* **2003**, *302*, 1545.
[22] S. M. Bachilo, M. S. Strano, C. Kittrell, R. H. Hauge, R. E. Smalley, R. B. Weisman, *Science* **2002**, *298*, 2361.
[23] R. B. Weisman, S. M. Bachilo, *Nano Lett.* **2003**, *3*, 1235.
[24] A. Hartschuh, H. N. Pedrosa, L. Novotny, T. D. Krauss, *Science* **2003**, *301*, 1354.
[25] M. Y. Sfeir, T. Beetz, F. Wang, L. M. Huang, X. M. H. Huang, M. Y. Huang, J. Hone, S. O'Brien, J. A. Misewich, T. F. Heinz, L. J. Wu, Y. M. Zhu, L. E. Brus, *Science* **2006**, *312*, 554.
[26] M. S. Dresselhaus, P. C. Eklund, *Adv. Phys.* **2000**, *49*, 705.
[27] H. Telg, J. Maultzsch, S. Reich, F. Hennrich, C. Thomsen, *Phys. Rev. Lett.* **2004**, *93*, 177 401.
[28] S. V. Goupalov, B. C. Satishkumar, S. K. Doorn, *Phys. Rev. B* **2006**, *73*, 115 401.
[29] Y.-Z. Ma, L. Valkunas, S. L. Dexheimer, S. M. Bachilo, G. R. Fleming, *Phys. Rev. Lett.* **2005**, *94*, 157 402.
[30] O. J. Korovyanko, C. X. Sheng, Z. V. Vardeny, A. B. Dalton, R. H. Baughman, *Phys. Rev. Lett.* **2004**, *92*, 017 403.
[31] C. Manzoni, A. Gambetta, E. Menna, M. Meneghetti, G. Lanzani, G. Cerullo, *Phys. Rev. Lett.* **2005**, *94*, 1.
[32] F. Wang, G. Dukovic, L. E. Brus, T. F. Heinz, *Science* **2005**, *308*, 838.
[33] J. Maultzsch, R. Pomraenke, S. Reich, E. Chang, D. Prezzi, A. Ruini, E. Molinari, M. S. Strano, C. Thomsen, C. Lienau, *Phys. Rev. B* **2005**, *72*, 241 402.
[34] H. Zhao, S. Mazumdar, C. X. Sheng, M. Tong, Z. V. Vardeny, *Phys. Rev. B* **2006**, *73*, 75 403.
[35] G. D. Scholes, G. Rumbles, *Nat. Mat.* **2006**, *5*, 683.
[36] Z. Wang, H. Pedrosa, T. Krauss, L. Rothberg, *Phys. Rev. Lett.* **2006**, *96*.

[37] T. Ando, *J. Phys. Soc. Jpn.* **1997**, *66*, 1066.
[38] C. L. Kane, E. J. Mele, *Phys. Rev. Lett.* **2004**, *93*, 197 402.
[39] C. D. Spataru, S. Ismail-Beigi, L. X. Benedict, S. G. Louie, *Phys. Rev. Lett.* **2004**, *92*, 774 021.
[40] H. B. Zhao, S. Mazumdar, *Phys. Rev. Lett.* **2004**, *93*, 157 402.
[41] V. Perebeinos, J. Tersoff, P. Avouris, *Phys. Rev. Lett.* **2004**, *92*, 257 402.
[42] E. Chang, G. Bussi, A. Ruini, E. Molinari, *Phys. Rev. Lett.* **2004**, *92*, 196 401.
[43] S. G. Chou, F. Plentz, J. Jiang, R. Saito, D. Nezich, H. B. Ribeiro, A. Jorio, M. A. Pimenta, G. G. Samsonidze, A. P. Santos, M. Zheng, G. B. Onoa, E. D. Semke, G. Dresselhaus, M. S. Dresselhaus, *Phys. Rev. Lett.* **2005**, *94*, 127 402.
[44] H. Htoon, M. J. O'Connell, P. J. Cox, S. K. Doorn, V. I. Klimov, *Phys. Rev. Lett.* **2004**, *93*, 027 401.
[45] X. H. Qiu, M. Freitag, V. Perebeinos, P. Avouris, *Nano Lett.* **2005**, *5*, 749.
[46] F. Plentz, H. B. Ribeiro, A. Jorio, M. S. Strano, M. A. Pimenta, *Phys. Rev. Lett.* **2005**, *95*, 247 401.
[47] C. Fantini, A. Jorio, M. Souza, M. S. Strano, M. S. Dresselhaus, M. A. Pimenta, *Phys. Rev. Lett.* **2004**, *93*, 147 406.
[48] H. Telg, J. Maultzsch, S. Reich, C. Thomsen, *Phys. Rev. B* **2006**, *74*, 115 415.
[49] A. Gambetta, C. Manzoni, E. Menna, M. Meneghetti, G. Cerullo, G. Lanzani, S. Tretiak, A. Piryatinski, A. Saxena, R. L. Martin, A. R. Bishop, *Nat. Phys.* **2006**, *2*, 515.
[50] Y. S. Lim, K. J. Yee, J. H. Kim, E. H. Haroz, J. Shaver, J. Kono, S. K. Doorn, R. H. Hauge, R. E. Smalley, *Nano Lett.* **2006**, *6*, 2696.
[51] B. J. LeRoy, S. G. Lemay, J. Kong, C. Dekker, *Nature* **2004**, *432*, 371.
[52] B. F. Habenicht, C. F. Craig, O. V. Prezhdo, *Phys. Rev. Lett.* **2006**, *96*, 187 401.
[53] V. Perebeinos, J. Tersoff, P. Avouris, *Phys. Rev. Lett.* **2005**, *94*, 027 402.
[54] M. T. Figge, M. Mostovoy, J. Knoester, *Phys. Rev. Lett.* **2001**, *86*, 4572.
[55] S. Tretiak, S. Kilina, A. Piryatinski, A. Saxena, R. L. Martin, A. R. Bishop, *Nano Lett.* **2007**, *7*, 86.
[56] J. Jiang, R. Saito, G. G. Samsonidze, S. G. Chou, A. Jorio, G. Dresselhaus, M. S. Dresselhaus, *Phys. Rev. B* **2005**, *72*, 235 408.
[57] M. Machon, S. Reich, C. Thomsen, *Phys. Rev. B* **2006**, *74*, 205 423.
[58] A. J. Heeger, S. Kivelson, J. R. Schrieffer, W. P. Su, *Rev. Mod. Phys.* **1988**, *60*, 781.
[59] S. Tretiak, S. Mukamel, *Chem. Rev.* **2002**, *102*, 3171.
[60] C. Wu, S. V. Malinin, S. Tretiak, V. Y. Chernyak, *Nat. Phys.* **2006**, *2*, 631.
[61] E. R. Batista, R. L. Martin, *J. Phys. Chem. A* **2005**, *109*, 9856.
[62] S. L. Dexheimer, A. D. VanPelt, J. A. Brozik, B. I. Swanson, *Phys. Rev. Lett.* **2000**, *84*, 4425.
[63] M. Klessinger, J. Michl, *Excited States And Photochemistry Of Organic Molecules*, VCH, New York **1995**.
[64] V. Balzani, F. Scandola, *Supramolecular Photochemistry*, Ellis Harwood, New York **1991**.
[65] G. Herzberg, *Molecular Spectra and Molecular Structure. I. Spectra of Diatomic Molecules*, 2nd ed., Van Nostrand Reinhold, New York **1950**.
[66] Y. Yin, A. N. Vamivakas, A. G. Walsh, S. B. Cronin, M. S. Unlu, B. B. Goldberg, A. K. Swan, *Phys. Rev. Lett.* **2007**, *98*, 037 404.
[67] A. P. Shreve, E. H. Haroz, S. M. Bachilo, R. B. Weisman, S. Tretiak, S. Kilina, S. K. Doorn, *Phys. Rev. Lett.* **2007**, *98*, 037 405.
[68] M. Machon, S. Reich, H. Telg, J. Maultzsch, P. Ordejon, C. Thomsen, *Phys. Rev. B Condens. Matter Mater. Phys.* **2005**, *71*, 35 416.
[69] M. T. Figge, M. Mostovoy, J. Knoester, *Phys. Rev. B* **2002**, *65*, 125 416.
[70] K. P. Bohnen, R. Heid, H. J. Liu, C. T. Chan, *Phys. Rev. Lett.* **2004**, *93*, 245 501.
[71] O. Dubay, G. Kresse, H. Kuzmany, *Phys. Rev. Lett.* **2002**, *88*, 235 506.
[72] G. Onida, L. Reining, A. Rubio, *Rev. Mod. Phys.* **2002**, *74*, 601.
[73] V. Perebeinos, J. Tersoff, P. Avouris, *Nano Lett.* **2005**, *5*, 2495.
[74] V. Perebeinos, J. Tersoff, P. Avouris, *Phys. Rev. Lett.* **2005**, *94*, 086 802.
[75] V. Perebeinos, J. Tersoff, P. Avouris, *Nano Lett.* **2006**, *6*, 205.
[76] V. Barone, J. E. Peralta, G. E. Scuseria, *Nano Lett.* **2005**, *5*, 1830.
[77] V. Barone, J. E. Peralta, M. Wert, J. Heyd, G. E. Scuseria, *Nano Lett.* **2005**, *5*, 1621.
[78] M. E. Casida, *Recent Advances in Density-Functional Methods. Part I*, Vol. 3, World Scientific, Singapore **1995**.
[79] L. Reining, A. Rubio, N. Vast, A. G. Marinopoulos, *Phys. Rev. Lett.* **2003**, *91*, 046 402.
[80] Z. Y. Zhou, M. Steigerwald, M. Hybertsen, L. Brus, R. A. Friesner, *J. Am. Chem. Soc.* **2004**, *126*, 3597.
[81] J. L. Brédas, J. Cornil, D. Beljonne, D. A. dos Santos, Z. Shuai, *Acc. Chem. Res.* **1999**, *32*, 267.
[82] G. R. Hutchison, Y. J. Zhao, B. Delley, A. J. Freeman, M. A. Ratner, T. J. Marks, *Phys. Rev. B* **2003**, *68*, 035 204.
[83] J. Gierschner, J. Cornil, H. J. Egelhaaf, *Adv. Mat.* **2007**, *19*, 173.
[84] S. Tretiak, *Nano Lett.* **2007**, *7*, 2201.
[85] S. Tretiak, A. Saxena, R. L. Martin, A. R. Bishop, *Phys. Rev. Lett.* **2002**, *89*, 097 402.
[86] S. Mukamel, S. Tretiak, T. Wagersreiter, V. Chernyak, *Science* **1997**, *277*, 781.
[87] S. Tretiak, A. Saxena, R. L. Martin, A. R. Bishop, *J. Phys. Chem. B* **2000**, *104*, 7029.
[88] I. Franco, S. Tretiak, *J. Am. Chem. Soc.* **2004**, *126*, 12 130.
[89] S. Tretiak, A. Saxena, R. L. Martin, A. R. Bishop, *Proc. Nat. Acad. Sci. USA* **2003**, *100*, 2185.
[90] M. J. S. Dewar, E. G. Zoebisch, E. F. Healy, J. J. P. Stewart, *J. Am. Chem. Soc.* **1985**, *107*, 3902.
[91] J. Ridley, M. C. Zerner, *Theor. Chim. Acta* **1973**, *32*, 111.
[92] R. E. Stratmann, G. E. Scuseria, M. J. Frisch, *J. Chem. Phys.* **1998**, *109*, 8218.
[93] F. Furche, R. Ahlrichs, *J. Chem. Phys.* **2002**, *117*, 7433.
[94] P. T. Araujo, S. K. Doorn, S. Kilina, S. Tretiak, E. Einarsson, S. Maruyama, H. Chacham, M. A. Pimenta, A. Jorio, *Phys. Rev. Lett.* **2007**, *98*, 067 401.
[95] J. J. P. Stewart, *MOPAC 2002*, Schrödinger Inc. and Fujitsu Limited, Portland, OR **2000**.
[96] S. Tretiak, A. Saxena, R. L. Martin, A. R. Bishop, *Chem. Phys. Lett.* **2000**, *331*, 561.
[97] A. Szabo, N. S. Ostlund, *Modern Quantum Chemistry: Introduction to Advanced Electronic Structure Theory*, McGraw-Hill, New York **1989**.
[98] E. R. Davidson, *Reduced Density Matrices in Quantum Chemistry*, Academic Press, New York **1976**.
[99] D. J. Thouless, *The Quantum Mechanics Of Many-Body Systems*, Academic Press, New York **1972**.
[100] P. Ring, P. Schuck, *The Nuclear Many-Body Problem*, Springer-Verlag, New York **1980**.
[101] J. Linderberg, P. Jorgensen, J. Oddershede, M. Ratner, *J. Chem. Phys.* **1972**, *56*, 6213.
[102] J. Linderberg, Y. Öhrn, *Propagators in Quantum Chemistry*, Academic Press, London **1973**.
[103] E. R. Davidson, *J. Comp. Phys.* **1975**, *17*, 87.
[104] S. Rettrup, *J. Comp. Phys.* **1982**, *45*, 100.
[105] D. Pines, D. Bohm, *Phys. Rev.* **1952**, *85*, 338.
[106] M. P. Allen, D. J. Tildesley, *Computer Simulation of Liquids*, Clarendon Press, Oxford **1987**.
[107] J. T. Frey, D. J. Doren, *TubeGen 3.3*, University of Delaware, Newark DE **2005**.
[108] A. Kokalj, *J. Mol. Graph. Model.* **1999**, *17*, 176.
[109] G. Scholes, S. Tretiak, T. McDonald, W. Metzger, C. Engtrakul, G. Rumbles, M. Heben, *J. Phys. Chem. C.* **2007**, *111*, 11 139.
[110] Z. M. Li, Z. K. Tang, H. J. Liu, N. Wang, C. T. Chan, R. Saito, S. Okada, G. D. Li, J. S. Chen, N. Nagasawa, S. Tsuda, *Phys. Rev. Lett.* **2001**, *87*, 127 401.
[111] H. Kuhn, *J. Chem. Phys.* **1948**, *16*, 840.
[112] H. Kuhn, *Helv. Chim. Acta* **1948**, *31*, 1441.
[113] H. Kuhn, *J. Chem. Phys.* **1949**, *17*, 1198.
[114] W. T. Simpson, *J. Am. Chem. Soc.* **1955**, *77*, 6164.

[115] R. Chang, J. H. Hsu, W. S. Fann, K. K. Liang, C. H. Chiang, M. Hayashi, J. Yu, S. H. Lin, E. C. Chang, K. R. Chuang, S. A. Chen, *Chem. Phys. Lett.* **2000**, *317*, 142.
[116] R. B. Capaz, C. D. Spataru, S. Ismail-Beigi, S. G. Louie, *Phys. Rev. B* **2006**, *74*, 121 401.
[117] I. D. W. Samuel, I. Ledoux, C. Dhenaut, J. Zyss, H. H. Fox, R. R. Schrock, R. J. Silbey, *Science* **1994**, *265*, 1070.
[118] R. E. Peierls, *Quantum Theory of Solids*, Clarendon, Oxford **1955**.
[119] E. F. Luis, F. Torres, S. Roche, *Phys. Rev. Lett.* **2006**, *97*, 076 804.
[120] P. M. Rafailov, J. Maultzsch, C. Thomsen, H. Kataura, *Phys. Rev. B* **2005**, *72*, 045 411.
[121] D. Connetable, G. M. Rignanese, J. C. Charlier, X. Blase, *Phys. Rev. Lett.* **2005**, *94*, 015 503.
[122] F. Plentz, H. B. Ribeiro, A. Jorio, M. S. Strano, M. A. Pimenta, *Phys. Rev. Lett.* **2005**, *95*, 247 401.